High-accuracy interferometry of extreme ultraviolet lithographic optical systems

Kenneth A. Goldberg[a] and Patrick Naulleau
Center for X-Ray Optics, Lawrence Berkeley National Laboratory, Berkeley, California 94720

Sang Lee
Center for X-Ray Optics, Lawrence Berkeley National Laboratory and EECS Department, University of California, Berkeley, California 94720

Cynthia Bresloff
Center for X-Ray Optics, Lawrence Berkeley National Laboratory, Berkeley, California 94720

Craig Henderson
Sandia National Laboratories, Livermore, California

David Attwood and Jeffrey Bokor
Center for X-Ray Optics, Lawrence Berkeley National Laboratory and EECS Department, University of California, Berkeley, California 94720

(Received 29 May 1998; accepted 16 September 1998)

Recent improvements in extreme ultraviolet (EUV) lithographic imaging with Schwarzschild objectives have come as a direct result of at-wavelength interferometric characterization with the phase-shifting point diffraction interferometer. High accuracy system wave front characterization has led to the determination of the best Schwarzschild objective and subaperture configuration. These investigations and the results of imaging experiments are discussed. Two pinhole null tests have provided an *in situ* method of demonstrating reference wavefront accuracy of $\sim\lambda_{EUV}/300$. [S0734-211X(98)15006-0]

I. INTRODUCTION

The phase-shifting point diffraction interferometer (PS/PDI) has been developed to meet the high demands of extreme ultraviolet (EUV) optical system wavefront measurements. Operating at a wavelength of 13 nm, these all-reflective multilayer-coated lithographic optical systems have fabrication and alignment tolerances in the subnanometer regime.[1] With numerical apertures (NAs) approaching 0.1, EUV lithographic optics are being designed for the 0.1 μm generation of lithographic pattern transfer.

The PS/PDI has been used in the *at-wavelength* characterization of 10× demagnification Schwarzschild objectives.[2,3] These investigations have included wavefront measurements of two different optical systems and, for one, the characterization of three separate subapertures. The first direct observations of chromatic vignetting and chromatic aberrations in EUV multilayers have been made using these systems.

Recent experiments demonstrate the utility of PS/PDI measurements in the prediction of imaging performance. Based on EUV system wavefront measurements and imaging experiments, these collaborative tests have driven the selection of the best available Schwarzschild objective and the specific subaperture and NA of that system that is available.

Interferometric measurement of and research conducted with Schwarzschild objectives serve several purposes. Capable of 0.1 μm pattern transfer, these are the highest resolution reflective optical systems presently available for EUV lithography research. As part of a collaboration between Lawrence Berkeley National Laboratory, Lawrence Livermore National Laboratory, Sandia National Laboratories (SNL), and industry, these optics are now being used at SNL in EUV imaging and resist development.[4] As more sophisticated optical systems are developed[5] EUV at-wavelength testing will comprise a critical step in the qualification process. At-wavelength interferometry may also play a role in the optical system alignment process. The series of interferometric experiments conducted over the past several years has been designed to evaluate and improve the performance of EUV interferometry, and to assure its availability as needed for testing the next generation of lithographic systems.

II. EXPERIMENT DESCRIPTION

The PS/PDI[6] generates spherical reference wave fronts by pinhole diffraction in the object and image planes of an optical system under test: one spherical beam coherently illuminates the system, while the second is compared to the test beam interferometrically. The pinhole-diffracted wave fronts enable the PS/PDI to achieve very high measurement accuracy. With its common-path design and limited number of components, the PS/PDI is relatively easy to implement and use.

A schematic design of the PS/PDI is shown in Fig. 1. A grating beamsplitter placed before the image plane, on either the object or the image side of the test optic, generates multiple focused beams that are spatially separated in the image plane. One beam containing the aberrations of the optical system is allowed to pass through a large window in an

[a]Electronic mail: KAGoldberg@lbl.gov

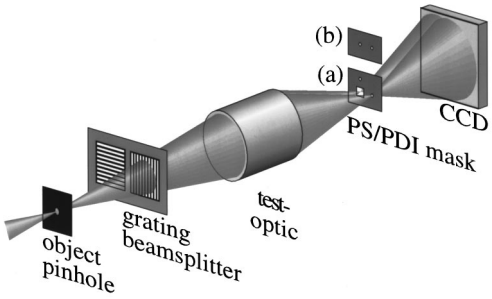

FIG. 1. Schematic representation of the key elements of the PS/PDI: (a) conventional pinhole mask, (b) two-pinhole null mask used in the calibration of the interferometer.

opaque membrane located in the image plane; this becomes the *test* beam. A second beam is brought to focus on a *reference pinhole*, smaller than the diffraction-limited resolution of the test optic, where it is spatially filtered to become a spherical *reference* beam covering the NA of measurement. A controllable phase shift between the test and reference beams is achieved by a simple lateral translation of the coarse grating beamsplitter. The test and reference beams propagate from the image plane to a detector where they overlap, producing the interference pattern. With or without reimaging optics, the detector is positioned to capture the NA of measurement.

A. 10× Demagnification Schwarzschild objective

The 10× Schwarzschild objective tested in these experiments is one of four Schwarzschild optics created to the same optical design specifications.[7] The optical design calls for two nested spherical mirror substrates, molybdenum–silicon multilayer coated, and optimized for peak reflectivity and performance at 13.4 nm wavelength. The coatings on the convex *primary* and concave secondary mirrors are graded to accommodate the angular range of the incident light. While the full optic has an annular pupil and cylindrical symmetry about its mechanical axis, only one off-axis subaperture is illuminated at a time. The unobstructed object-side and image-side NAs of 0.008 and 0.08, respectively, are defined by a removable aperture stop that rests against the primary mirror (Fig. 2). The optic is designed to have a circular, 400-μm-diam field of view in the image plane, with a 1 μm depth-of-focus.

During assembly, the magnitude and type of the EUV wave front aberrations were not yet known. A strategy was adopted wherein the optic was given an entrance pupil with three differently sized apertures as shown in Fig. 2. The removable aperture stop separately defines 0.06, 0.07, and 0.08 NA apertures and occupies a plane normal to the mechanical axis of the optic. For the particular optic described here, the largest subaperture (A) is unusable due to its noncircular shape.

The optic was designed to be used in the vertical orientation with the image plane at the top of the mechanical housing. In imaging applications the wafer, with photoresist facing downward, rests on three steel balls. Because the optic is designed to be used in this vertical orientation, and any change could introduce mechanical deformations to the mirror substrates, all EUV interferometric tests are performed vertically with the optic illuminated from below.

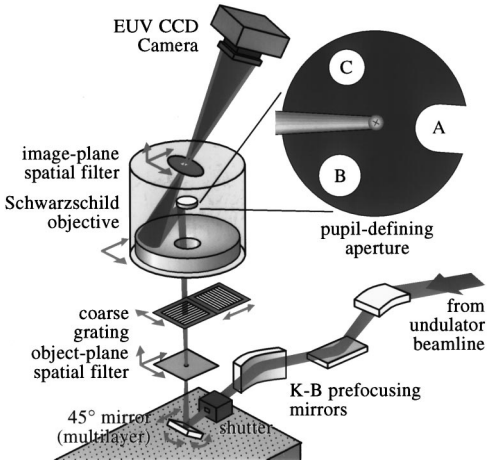

FIG. 2. Configuration of the EUV PS/PDI used in the measurement of a 10× Schwarzschild objective. A rotatable aperture stop, expanded here for clarity, rests against the primary mirror and defines three separate off-axis subapertures. Here, the 0.08, 0.07, and 0.06 NA subapertures are labeled A, B, and C, respectively. Measurements are performed at the Advanced Light Source.

B. Interferometric testing

The experimental configuration and procedure for interferometric testing have been described previously[3,8] and are discussed here only briefly. This configuration is shown schematically in Fig. 2. Tests are performed using an undulator beamline[9] at the Advanced Light Source synchrotron radiation facility at Lawrence Berkeley National Laboratory. The beamline provides a tunable source of EUV radiation with a spectral bandwidth $\lambda/\Delta\lambda$ of 200–1000 at 13.4 nm wavelength. Up to 33 μW (1.7×10^{12} photons/s) of coherent flux[10] can be delivered through a 0.75-μm-diam pinhole that serves as the entrance pinhole spatial filter for the interferometer.

A transmission grating beamsplitter is placed between the object pinhole and the test optic, approximately 60 mm above the object pinhole. The 18-μm-pitch grating is made of a gold absorber pattern on a 100-nm-thick silicon–nitride membrane, with 0.5×0.5 cm^2 area. The grating is held on a one-dimensional horizontal translation stage, with motion in the direction perpendicular to the rulings, to enable phase shifting. An identical complementary grating stage is used to insert a second grating, mounted at 90° to the first. This enables rotation of the beam separation, and concomitantly the fringe pattern, by 90°.

With the beam and object pinhole held stationary, alignment of the image point within the image plane is performed by a two-axis lateral translation of the test optic. This translation with respect to a stationary object point takes advantage of the 10× demagnification to enable positioning of the image point with better than 0.1 μm resolution.

During the PS/PDI development, reference pinhole (image plane) masks have been fabricated by several different

means with pinhole diameters between 60 and 200 nm. Pinholes used in the interferometry experiments described here were fabricated with focused ion beam lithography, and consist of 240 nm of an indium–antimonide absorber on a 100 nm silicon–nitride support membrane. Subsequent experiments, including the null-test accuracy measurements, have been performed using 50–100-nm-diam pinholes fabricated with electron-beam lithography.[11] Typically, an array of pinholes in the mask is used to cover a range of field points.

Data is recorded with a back-thinned, back-illuminated, charge coupled device (CCD) detector with 1 in.^{2} area. The CCD is mounted at an angle of 12° from the vertical to receive the central ray at normal incidence.

III. ACCURACY VERIFICATION

Significant effort has been directed toward understanding both the precision and the accuracy of the PS/PDI under various configurations. Precision relies on the stability of the components, the repeatability of the measurements, and the number of samples averaged together, and can be inferred from the variation in a set of measurements. Measurement accuracy relies on the identification and removal of systematic error sources, and includes the quality of the pinhole-diffracted wavefronts. Accuracy verification requires a different experimental approach. Previously, semiquantitative accuracy verification has come from imaging experiments.[3] Recently, two-pinhole *null tests*[8] have been used to measure accuracy as a function of the reference pinhole size and the NA of measurement.

For these two-pinhole null tests, the image-plane window that transmits the test beam is replaced by a second reference pinhole [Fig. 1(b)] for a measurement that is reminiscent of Young's experiment. Rotation and longitudinal translation of the grating beamsplitter are required to produce a beam separation that matches the reference pinhole pair.

Analysis of the resultant interference patterns reveals a small geometric systematic error that arises from the fact that the interference occurs between two, laterally displaced, nominally spherical beams.[8] This error is easily predicted and subtracted during analysis. The presence of any other residual components in the measured path-length difference is attributable to nonspherical components in the diffracted reference waves. Considering many similar pinhole pairs and a range of intentionally varied illumination conditions provides a method to assess the accuracy present during optical testing.

Figure 3 shows a typical interferogram from a two-pinhole null test using pinholes with an apparent diameter of 100 nm. In practice, the diameter of the reference pinholes is difficult to measure; this is primarily due to their small size and potentially nonuniform cross section. The *apparent* pinhole sizes are based on comparisons of the measured diffraction profiles with those predicted by scalar diffraction theory: *Airy* diffraction from ideal circular apertures.

As expected, the measurement accuracy improves with a reduction in pinhole size, and a resultant improvement in spatial filtering. Furthermore, the quality of the reference wavefront has been observed to be limited by incomplete spatial filtering of the aberrated wavefront produced by the optic under test, rather than by physical pinhole diffraction limits. One significant consequence of this property is the prediction that measurement accuracy will improve with a corresponding improvement in the quality of the optic under test. This behavior is a natural result of the fact that the PS/PDI generates its reference wavefront by spatially filtering the aberrated test beam.

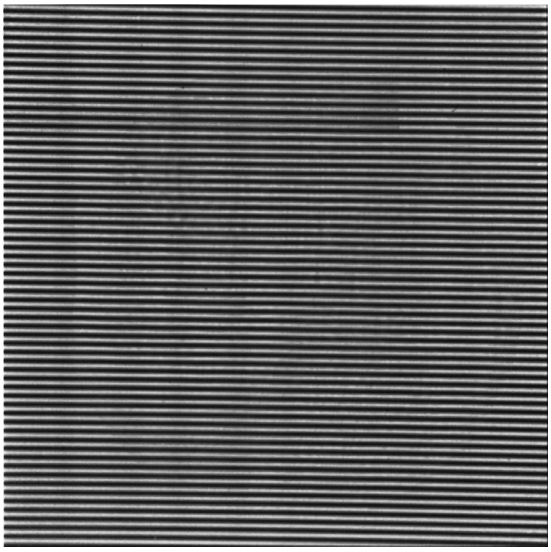

FIG. 3. Typical interferogram recorded during two-pinhole null-test measurements. Shown here is the pattern from two 100 μm pinholes. These tests are used to characterize systematic measurement effect.

Table I shows three equivalent measures of the reference wave front root mean square (rms) error as a function of the apparent pinhole size, compiled from a large number of two-pinhole null-test measurements. The Schwarzschild objective used in these measurements has an EUV wave front quality of 0.164 waves rms, at 0.08 NA.

IV. WAVEFRONT MEASUREMENT AND IMAGING PERFORMANCE

The three separate subapertures of one 10× Schwarzschild objective were measured interferometrically and two subapertures have been successfully used in EUV lithographic imaging experiments. This section describes the wave front measurements and the improvement in imaging performance that has come as a result of conclusions based on at-wavelength interferometry. The interferogram analysis

TABLE I. Measured reference wavefront quality at 0.08 NA.

Apparent pinhole size (nm)	Reference wavefront rms error		
	(waves)	(nm)	(waves^{-1})
80	0.0030±0.0002	0.040±0.003	333
100	0.0040±0.0003	0.054±0.004	250
120	0.0099±0.0007	0.133±0.009	101
140	0.0120±0.0005	0.161±0.007	83

and wavefront phase retrieval methods used consist of phase-shifting interferometry techniques optimized for these applications. Detailed descriptions of these methods have been presented elsewhere.[12]

A. Wavefront measurement in three subapertures

Wavefront measurements have been performed for all three of the available subapertures. Similarities among the three measurements suggest the presence of an overall *zonal* fabrication error along the annular full aperture.

Originally, most attention was paid to subaperture B, with an NA of 0.07, and 0.099 ± 0.008 waves rms of aberration. Imaging experiments performed with this aperture verified the predicted performance.[3] Subsequently, careful consideration of the wavefront data recorded in subaperture C led to the selection of that subaperture as the best available. These measurements were performed with the pupil-defining aperture removed, revealing a large area of the annulus, shown in Fig. 4. Having wave front data over an extended area enables the prediction of optical performance as a function of the position or size of the aperture stop. This is achieved by numerically masking the acquired data during the analysis process; in this way the optimal configuration for subaperture C was determined.

The results of these calculations are shown in Fig. 5. For each NA, available aperture stop positions were considered only if 95% or more of the points within the appropriate circular domain were valid measured points of the phasemap. This requirement excluded points from the inner and outer edges of the annulus, and points at the top and bottom rotational positions in the domain. Because of its relatively large size within the domain, the calculations performed for 0.08 NA are limited to a small translation region. For each NA, the single $\times$ indicates the center of the original 0.06 NA aperture stop. Within the observable area, these measurements show that the original placement of the aperture stop is close to the position of minimum wave front rms error. Unfortunately, with the minimum occurring at the domain edge, it is not clear if these positions represent global ''sweet spots'' of minimum wave front aberration, or local minima of the limited measurement domain.

Figures 5(d) and 5(e) show the rms wave front error as a function of the rotational orientation of the aperture stop for three NA values, and for a circular region concentric with the original aperture position. The rotation-only calculation [Fig. 5(d)] shows that the improvement gained by rotation is not more than a few percent. Figure 5(e) reveals the compromise that must be made between NA and wavefront quality. Detailed predictions of imaging performance are required to evaluate the optimal NA value in this situation.

B. Imaging

EUV interferometric characterization led to the selection of subaperture C as the best candidate for imaging. To test the validity of this determination, the imaging system was modified to use subaperture C at 0.06 NA (0.048 waves rms error) instead of subaperture B at 0.07 NA (0.099 waves rms error). This led to improvements in several imaging characteristics including astigmatism and depth of focus. The line-edge roughness in resist images, however, was seen to degrade slightly for smaller features due to the reduced NA.

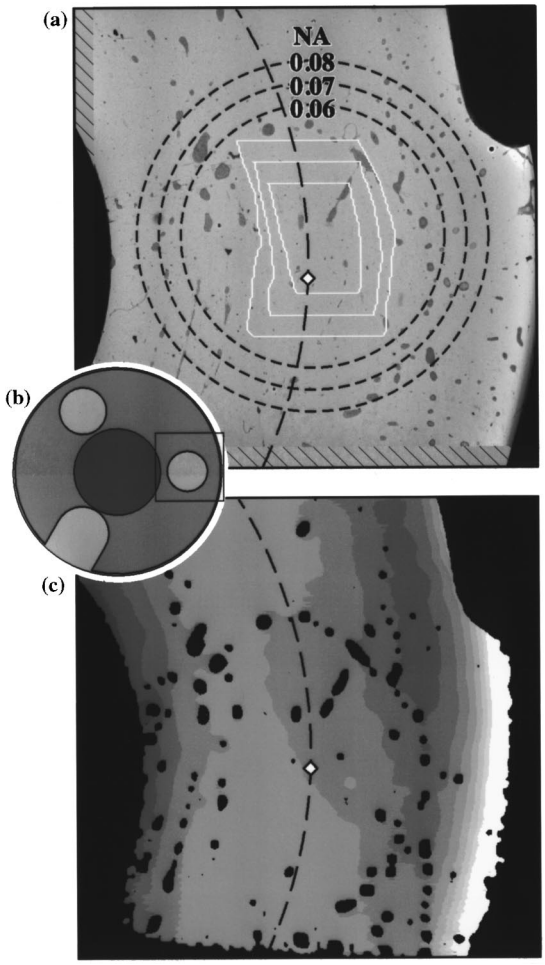

FIG. 4. The intensity and the phase responses of subaperture C of the Schwarzschild objective's annular pupil are under investigation. The region depicted in (a) and (c) is outlined by a square in (b). (a) An image of the reflective area of the pupil, scaled for display, reveals numerous 100 μm scale blemishes in the mirror surfaces. Three circular rings illustrate the relative sizes and coverage of three numerical aperture values. (c) A wavefront phasemap calculated interferometrically. Gradations in the gray level indicate filled contours of 0.1 waves at 13.4 nm wavelength. The diamond symbol indicates the original center of the 0.06 NA aperture, while the dashed arc shows the aperture positions available by rotation of the aperture stop. Three nested white outlines in (a) bound the regions over which the aperture *centers* may be placed for the position-dependent calculations. The largest region bounds the 0.06 NA aperture center, while the smallest is for 0.08 NA.

As described above, however, the interferometry and subsequent simulation also predicted good performance for the case where the aperture stop in subaperture C of the optic is expanded to an NA of 0.07 (0.061 waves rms error). In order to achieve this expanded NA, the aperture stop was rotated axially by 120° to bring the 0.07 NA pupil to the position of subaperture C on the optic. This configuration proved to be the optimal imaging configuration for this optic. Table II compares the line-edge roughness for subaperture C before and after expansion to an NA of 0.07. The line-edge roughness values are 1σ, one side, taken from lines printed at a 1:1 pitch with a wavelength of 13.4 nm in top surface imaging

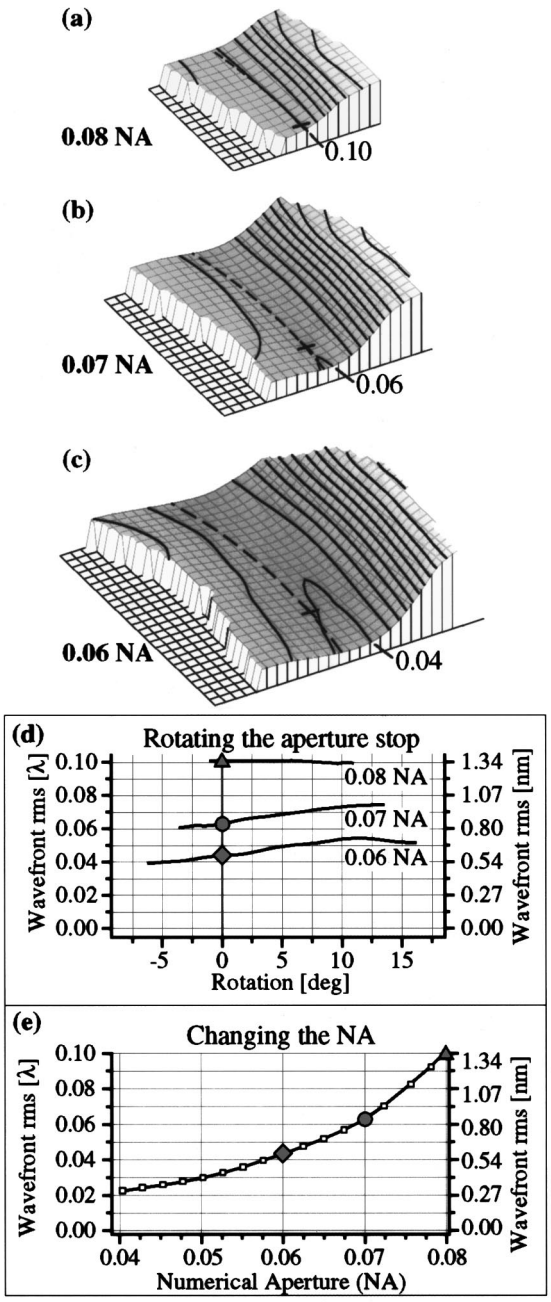

FIG. 5. (a)–(c) Position-dependent analysis of the wavefront rms for three NA values. Contours are spaced at 0.02 waves at 13.4 nm wavelength. × indicates the original center position of the aperture. Positions available by rotation are indicated by the dashed arc. Wavefront rms values along these arcs are shown in (d). For apertures placed concentric with the original position, the relationship between wavefront rms and numerical aperture is shown in (e).

resist.[13] The line-edge roughness improvement for feature sizes of 150 nm and smaller is evident. EUV interferometry has predicted the best of the three available subapertures and determined that a performance enhancement by NA enlargement in this subaperture would not be offset by increased aberration magnitude.

V. CONCLUSION

The importance of at-wavelength EUV interferometric measurements to qualifying EUV lithographic optical systems has been demonstrated. With an accuracy of 0.040 nm over a NA of 0.08, EUV system wave front measurements have played a vital, guiding role in the recent success of EUV imaging experiments. This capability is ready to address the qualification needs of more sophisticated EUV lithographic systems. Furthermore, the PS/PDI accuracy is more than adequate to perform at-wavelength alignment of these systems.

TABLE II. Line-edge roughness values (1σ, one side) at subaperture C as a function of NA measured for lines printed at 1:1 pitch with at a wavelength of 13.4 nm.

Linewidth (nm)	Line-edge roughness (nm)	
	NA = 0.06	NA = 0.07
200	3.44	3.74
175	3.53	4.08
150	4.93	4.11
130	5.45	3.80
120	5.83	3.59
100	10.70	4.03

ACKNOWLEDGMENTS

The authors wish to acknowledge the contributions of Hector Medecki and Edita Tejnil in the at-wavelength wavefront measurements; also Paul Denham and Phil Batson for engineering and technical support essential to the success of this work. Finally, they wish to thank Avi Ray-Chaudhuri of Sandia National Laboratories for providing imaging simulation support. This work, performed at the Lawrence Berkeley National Laboratory, was supported by the Extreme Ultraviolet Limited Liability Company (EUV LLC), the SRC, the DARPA Advanced Lithography Program, and by the Office of Basic Energy Sciences of the U.S. Department of Energy.

[1]D. M. Williamson, in *OSA Proceedings on Extreme Ultraviolet Lithography* (Optical Society of America, Washington, DC, 1994), Vol. 23, pp. 68–76.
[2]K. A. Goldberg, E. Tejnil, S. H. Lee, H. Medecki, D. T. Attwood, K. H. Jackson, and J. Bokor, Proc. SPIE **3048**, 264 (1997).
[3]E. Tejnil *et al.*, J. Vac. Sci. Technol. B **15**, 2455 (1997).
[4]J. Goldsmith *et al.*, Proc. SPIE **3331**, 11 (1998).
[5]D. Sweeney, R. Hudyma, H. N. Chapman, and D. Shafer, Proc. SPIE **3331**, 2 (1998).
[6]H. Medecki, E. Tejnil, K. A. Goldberg, and J. Bokor, Opt. Lett. **21**, 1526 (1996).
[7]D. Tichenor *et al.*, in *OSA Proceedings on Soft X-Ray Projection Lithography*, edited by A. M. Hawryluk and R. H. Stulen (Optical Society of America, Washington, DC, 1993), Vol. 18, pp. 79–82.
[8]P. Naulleau, K. A. Goldberg, S. H. Lee, C. Chang, C. Bresloff, P. Batson, D. Attwood, and J. Bokor, Proc. SPIE **3331**, 114 (1998).
[9]R. Beguiristain, J. Underwood, M. Koike, B. Batson, E. Gullickson, K. Jackson, H. Medecki, and D. Attwood, Proc. SPIE **2855**, 159 (1997).
[10]D. Attwood, G. Sommargren, R. Beguiristain, K. Nguyen, J. Bokor, N. Ceglio, K. Jackson, M. Koike, and J. Underwood, Appl. Opt. **32**, 7022 (1993).
[11]E. Anderson, V. Voegli, and L. Murray, J. Vac. Sci. Technol. B **13**, 2529 (1995).
[12]K. A. Goldberg, Ph.D. dissertation, University of California, Berkeley, 1997.
[13]C. Henderson, D. Wheeler, T. Pollagi, D. O'Connell, J. Goldsmith, A. Fisher, G. Cardinale, J. Hutchinson, and V. Rao, Proc. SPIE **3331**, 32 (1998).